Chapter 4
LEAP-UCD-2017 Comparison of Centrifuge Test Results

Bruce L. Kutter, Trevor J. Carey, Nicholas Stone, Bao Li Zheng, Andreas Gavras, Majid T. Manzari, Mourad Zeghal, Tarek Abdoun, Evangelia Korre, Sandra Escoffier, Stuart K. Haigh, Gopal S. P. Madabhushi, Srikanth S. C. Madabhushi, Wen-Yi Hung, Ting-Wei Liao, Dong-Soo Kim, Seong-Nam Kim, Jeong-Gon Ha, Nam Ryong Kim, Mitsu Okamura, Asri Nurani Sjafruddin, Tetsuo Tobita, Kyohei Ueda, Ruben Vargas, Yan-Guo Zhou, and Kai Liu

B. L. Kutter (✉) · T. J. Carey · N. Stone · B. L. Zheng · A. Gavras
Department of Civil and Environmental Engineering, University of California, Davis, CA, USA
e-mail: blkutter@ucdavis.edu

M. T. Manzari
Department of Civil and Environmental Engineering, George Washington University, Washington, DC, USA

M. Zeghal · T. Abdoun · E. Korre
Department of Civil and Environmental Engineering, Rensselaer Polytechnic Institute, Troy, NY, USA

S. Escoffier
IFSTTAR, GERS, SV, Bouguenais, France

S. K. Haigh · G. S. P. Madabhushi · S. S. C. Madabhushi
Department of Engineering, Cambridge University, Cambridge, UK

W.-Y. Hung · T.-W. Liao
Department of Civil Engineering, National Central University, Taoyuan, Taiwan

D.-S. Kim
Department of Civil and Environmental Engineering, Korea Advanced Institute of Science and Technology, Daejeon, South Korea

S.-N. Kim
Water Management Department, Korea Advanced Institute of Science and Technology, Daejeon, South Korea

J.-G. Ha
Korea Advanced Institute of Science and Technology, Yuseong, South Korea

N. R. Kim
K-water Research Institute, Korea Water Resources Corporation, Daejeon, South Korea

M. Okamura · A. N. Sjafruddin
Department of Civil Engineering, Ehime University, Matsuyama, Japan

B. Kutter et al. (eds.), *Model Tests and Numerical Simulations of Liquefaction and Lateral Spreading*, https://doi.org/10.1007/978-3-030-22818-7_4

Abstract This paper compares experimental results from every facility for LEAP-UCD-2017. The specified experiment consisted of a submerged medium-dense clean sand with a 5-degree slope subjected to 1 Hz ramped sine wave base motion in a rigid container. The ground motions and soil density were intentionally varied from experiment to experiment in hopes of defining the slope of the relational trend between response (e.g., displacement, pore pressure), intensity of shaking, and density or relative density. This paper is also intended to serve as a useful starting point for overview of the experimental results and to help others find specific experiments if they want to select a subset for further analysis. The results of the experiments show significant differences between each other, but the responses show a significant correlation, $R^2 \sim 0.7$–0.8, to the known variation of the input parameters.

4.1 Introduction

Twenty-four separate model tests were conducted at nine different centrifuge facilities for this LEAP exercise. The first goal of this paper is to provide an overview of all the experimental data from the 24 experiments. This overview will allow readers to quickly scan through the key time series data and various performance measures to evaluate the extent of liquefaction in the different experiments. A second goal of this paper is to demonstrate that the experiments are consistent with each other and that they define a response function or trend between key input parameters and key liquefaction response parameters. From the comparison of the results to empirical response functions, it is possible to obtain meaningful assessments of the sensitivity of the results to variations of input parameters and to assess the variability of the results in terms of their deviation from the response functions.

All of the experiments were intended to model a 4 m-deep, 20 m-long prototype soil deposit of submerged uniform sand with a 5-degree surface slope instrumented as indicated in Fig. 4.1. This paper attempts to compare the results from all of the first shaking events of each model test. The same sand, Ottawa F65 from US Silica, was used in all of the experiments. Carey et al. (2019c) describe results of grain size and max/min density tests of the sand used at different facilities to determine the index properties and to check the consistency of the sand used at various facilities.

El Ghoraiby et al. (2017) and Para Bastidas et al. (2017) report results of laboratory testing including cyclic triaxial and DSS tests. Permeability tests using

T. Tobita
Institute of Geotechnical Engineering, Zhejiang University, Hangzhou, China

K. Ueda · R. Vargas
Disaster Prevention Research Institute, Kyoto University, Kyoto, Japan

Y.-G. Zhou
Department of Civil Engineering, Zhejiang University, Hangzhou, P. R. China

K. Liu
Department of Civil Engineering, Kansai University, Suita, Japan

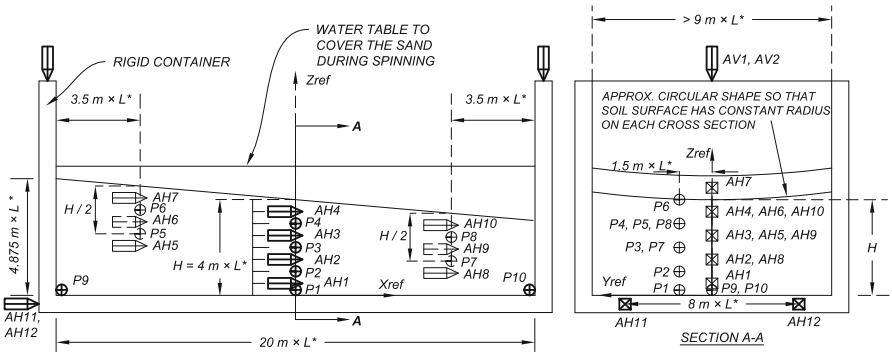

Fig. 4.1 Configuration of all of the model tests as specified by Kutter et al. (2019)

Table 4.1 Test facilities, length scale factor, shaking direction, radius of centrifuge, and model container length/width ratio for LEAP-UCD-2017

Centrifuge facility institution	L^*	Shaking direction	Radius (m)	Container length/ width
Cambridge University, UK	1/40	Tangential	3.56	0.45
Ehime University, Japan	1/40	Parallel to axis	1.184	0.24
IFSTTAR, France	1/50	Parallel to axis	5.063	0.5
KAIST, Rep. of Korea	1/40	Parallel to axis	5	0.45
Kyoto University, Japan	1/44.4	Tangential	2.5	0.32
National Central Univ., Taiwan	1/26	Parallel to axis	2.716	0.45
Rensselaer Poly. Inst., USA	1/23	Parallel to axis	2.7	0.42
Univ. of California, Davis, USA	1/43.75	Tangential	1.094	0.63
Zhejiang University, China	1/30	Parallel to axis	4.315	0.59

water as the pore fluid as reported by El Ghoraiby et al. (2017) were fit with a linear regression line through data over the range of $e = 0.5$–0.75:

$$k = (0.0207(e) - 0.0009)\ \text{cm/s} \tag{4.1}$$

As the pore fluid viscosity was scaled in the centrifuge tests, this measured permeability corresponds to the prototype permeability.

Some basic parameters including the institutions and direction of shaking for the nine centrifuge facilities are summarized in Table 4.1. The table also shows that the scale factor selected for the model tests ($L^* = L_{\text{model}}/L_{\text{prototype}}$) varied from 1/50 to 1/23, and the radii varied between 1 and 5 m. The models were all tested in a rigid model container to avoid the uncertainties associated with more complex flexible model containers. To control side boundary effects, Kutter et al. (2019) recommended 0.45 as a minimum desired width/length ratio of the model container; the actual width/length ratios are summarized in Table 4.1.

4.2 Densities and Penetration Resistances

Each experimental facility was given suggestions regarding target densities and target input motions for the first shaking event; each site was given some latitude in deciding what input motions to apply in subsequent shaking events, if any. The details of results for all the shaking events should be described in separate papers produced by each experimental facility. The density of the sand in each model was characterized by mass and volume measurements of each model. However, it is deceptively difficult to directly measure the mass and volume to the desired level of accuracy. Small errors due to sand mounding near the container side walls during pluviation, imperfect container rectangularity, and uneven (rough) surfaces at the base and top of the sand deposit, in combination with resolution and accuracy of the load cells used to measure the weight of the sand and the empty container, contribute to the uncertainty of the mass and volume measurement. Also note that the relative density is very sensitive to density; at $D_r = 60\%$, a 1% error in density results in a 6% error in relative density.

For an independent check on the density, new 6 mm-diameter cone penetrometers were developed and manufactured at UC Davis (Carey et al. 2018b, 2019a) and then distributed to the centrifuge sites. The penetrometers had different rod lengths but were otherwise identical. Cone penetration tests were to be performed at the test acceleration prior to each destructive shaking event for every test site. At Cambridge, the centrifuge was spun up, the penetration test was performed, the ground motion was triggered, and finally a second CPT was pushed in the same location of the model all during the same spin, without stopping the centrifuge. For all other sites, the centrifuge was spun up to the test acceleration ($g^* = 1/L^*$) for a penetration test and then stopped for removal of the penetrometer. Then the centrifuge was spun up to the test acceleration to apply the model earthquake. Subsequent penetration tests were done at different locations in subsequent spins. Figure 4.2 shows cone penetration tests for every model test. Blank figures indicate unsuccessful penetration tests.

Since the same cone design and the same sand were used at different centrifuge facilities, the results should be comparable. However, the length scale factor in the centrifuge tests varies between 1/23 and 1/50, so the prototype diameter of the cone varies between 138 and 300 mm. At mid depth of the 4 m-thick prototype layer, the depth/diameter ratio varied between 6.7 and 14.5. Bolton et al. (1999) indicated that for dense specimens (D_r~80%) the normalized penetration distance was not sensitive to depth if depth/diameter is greater than about 10. For LEAP, we may expect minor reductions of normalized penetration resistance for cases where depth/diameter < 10. Carey et al. (2019a) observed about 5–10% greater penetration resistance for low g tests (large depth/diameter) compared to high g tests.

Bolton et al. (1999) also identified an effect of the container width on the penetration resistance. Narrow containers produced about 15–20% increase in

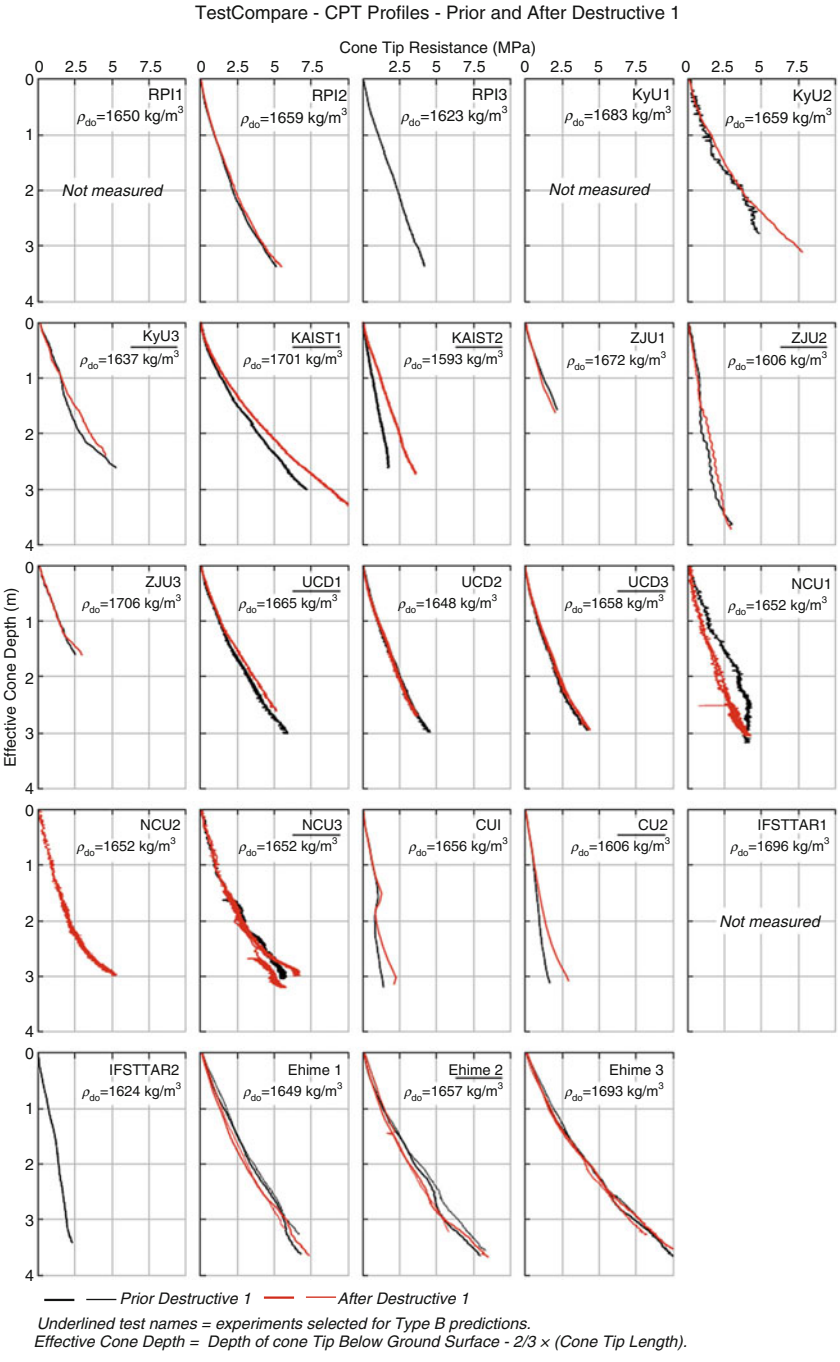

Fig. 4.2 CPT profiles before the first destructive ground motion

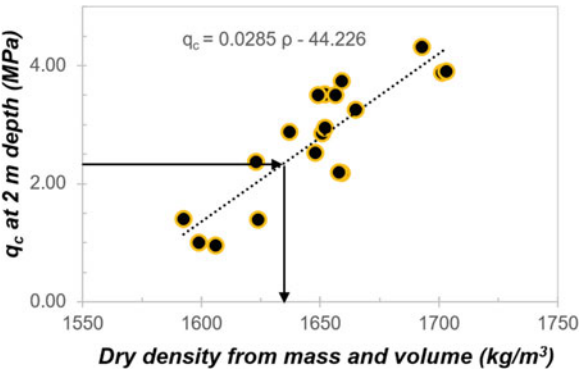

Fig. 4.3 Correlation between q_c and dry density from CPT tests

penetration resistance. In addition to producing an increased penetration resistance for a given density, wall friction from narrow containers would also restrict liquefaction deformations for a given density; these errors are expected to counteract each other to some extent. Effects of container width on penetration resistance were not accounted for in the correlations presented later in this paper.

As will be demonstrated later, the cone penetration resistance at a 2 m depth is more highly correlated to the liquefaction behavior than is the density determined by mass and volume measurements. For this paper, the dry density was determined by least squares fit to the data shown in Fig. 4.3. The inverse form of the equation of the regression line indicated in Fig. 4.3 is $\rho_d = a(q_c) + b$, with a = 35.1 kg/m^3/MPa and b = 1553 kg/m^3. As indicated by the arrows in the figure, one model was reported to have a density based on mass and volume measurements of 1623 kg/m^3 and a q_c(2 m) = 2.37 MPa. At the intersection of q_c(2 m) = 2.37 MPa and the regression line one finds that the dry density from q_c is $\rho_d(q_c(2\text{ m})) = 1636$ kg/m^3.

4.3 Base Input Motions in First Destructive Motion

Figure 4.4 shows an example of a horizontal base input motion for test UCD3. Ideally the input motions would have been a smooth ramped sine wave similar to the top trace of Fig. 4.4. While every centrifuge shaker used in LEAP produced motions that contained the ramped sine wave, they also produced high-frequency accelerations superimposed on the ramp. In Fig. 4.4, the bottom trace is the actual achieved base acceleration recorded in the UCD3 test. The top trace of Fig. 4.4 shows the low-frequency (approx. 1 Hz) component of the achieved motion (the portion passed through a 0.5–1.2 Hz band-pass filter); the middle trace is the high-frequency component of the base motion determined by subtracting the low-frequency component from the achieved base motion.

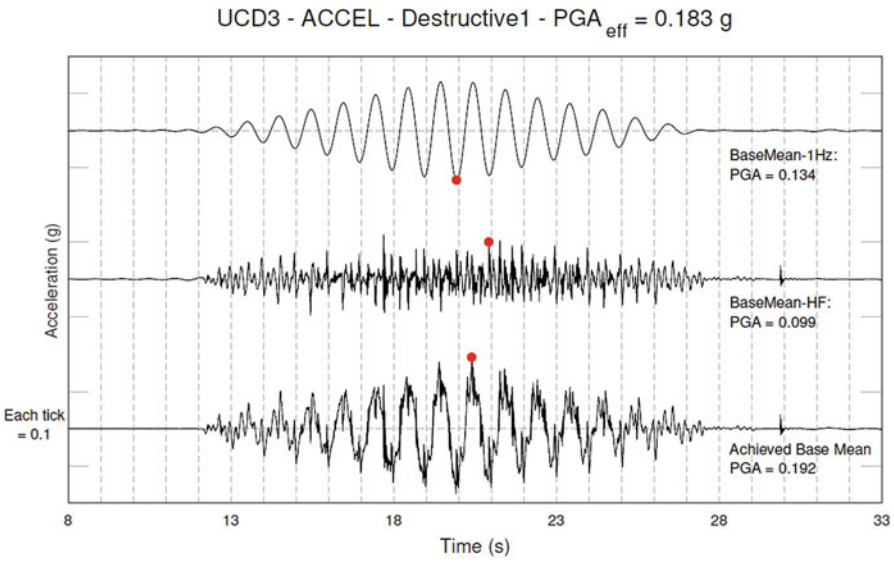

Fig. 4.4 Example from test UCD3 of a horizontal base input motion and an illustration of the method to determine PGA_{eff}

As a measure of the intensity of the achieved input motion, one may use the PGA, the PGA of the low-frequency component (PGA_{1Hz}), the PGA of the high-frequency component, or traditional intensity measures such as the PGV, the Arias intensity (I_a), or cumulative absolute velocity (CAV_5). For the purposes of organizing and comparing the LEAP experiments, another parameter, PGA_{eff}, was found to be useful:

$$PGA_{eff} = PGA_{1Hz} + 0.5\ PGA_{HF} \tag{4.2}$$

where PGA_{HF} is determined from the peak of the high-frequency component that occurs within 1 s of the peak of the PGA_{1Hz}. (Note that the larger peak of the high-frequency component at about 17.7 s in Fig. 4.4 was not used because it was not near the PGA of the 1 Hz component.)

Table 4.2b summarizes the intensity measures for each of the first destructive motions for each experiment. It should be emphasized that many of the LEAP experiments included a total of two or three destructive motions. This paper focuses on results from the first motion only. Papers by each experiment facility explain the results from subsequent destructive motions.

To allow for a qualitative comparison of the input motions, Fig. 4.5 presents time histories from the horizontal base motions AH11 and AH12 and from the vertical accelerometers AV1 and AV2. The top trace in each subplot shows the measured

Table 4.2a Summary of density measures for each of the models

Test ID	Dry density from mass and volume ρ(M&V) [1]	D_r(M&V) assuming $\rho_{max} = 1757$, $\rho_{min} = 1490.5$ [2]	Pen. Resist. at 2 m depth q_c(2 m) [3]	$\rho(q_c(2\text{ m})) = a\ q_c + b$ a = 35.1; b = 1553 [4]	D_r from q_c ρ from [4] and $\rho_{max} = 1757$ $\rho_{min} = 1490.5$ [5]
	kg/m^3		MPa	kg/m^3	
CU1	1656	0.66	0.81	1581	0.38
CU2	1606	0.47	0.95	1586	0.40
Ehime1	1649	0.63	3.50	1676	0.73
Ehime2	1657	0.66	3.50	1676	0.73
Ehime3	1693	0.79	4.31	1704	0.83
IFSTTAR1	1696	0.80			
IFSTTAR2	1624	0.56	1.38	1602	0.46
KAIST1	1701	0.82	3.88	1689	0.77
KAIST2	1593	0.42	1.40	1602	0.46
KyU1	1683	0.75			
KyU2	1659	0.67	3.74	1684	0.76
KyU3	1637	0.59	2.88	1654	0.65
NCU1	1652	0.64	3.51	1676	0.73
NCU2	1652	0.64			
NCU3	1652	0.64	2.95	1656	0.66
RPI1	1650	0.64			
RPI2	1659	0.67	2.18	1630	0.56
RPI3	1623	0.54	2.37	1636	0.59
UCD1	1665	0.69	3.26	1667	0.70
UCD2	1648	0.63	2.52	1642	0.61
UCD3	1658	0.67	2.19	1630	0.56
ZJU1	1651	0.64	2.85	1653	0.65
ZJU2	1599	0.45	1.00	1588	0.41
ZJU3	1703	0.82	3.90	1690	0.78

horizontal base velocities obtained by time integration of the data from AH11 and AH12. The bottom trace in each subplot shows the high-frequency component of the base acceleration, and the second trace from the bottom shows the 1 Hz component of the base motion.

Figure 4.5 shows that the base motion for test UCD2 contains several large-amplitude sharp spikes, IFSTTAR1 has more continuous high-frequency components, and CU1, CU2, and RPI2 contain significant 3 Hz components superimposed on the motion. RPI2 motion was intentionally varied to allow emulation of the high-frequency component observed in the CU experiments. The first few and last few

Table 4.2b Summary of ground motion intensity measures for the first destructive shake

Test ID	PGA	PGA_{eff}	PGA_{1Hz}	PGA_{HF}	PGV	Cumulative abs. vel. CAV_5	Arias intensity I_a
	g	g	g	g	m/s	m/s	m^2/s
CU1	0.190	0.186	0.123	0.125	0.253	7.75	1.20
CU2	0.206	0.195	0.122	0.146	0.259	8.04	1.31
Ehime1	0.169	0.158	0.135	0.045	0.202	8.26	1.07
Ehime2	0.180	0.158	0.134	0.048	0.206	8.25	1.07
Ehime3	0.168	0.155	0.136	0.039	0.200	8.24	1.07
IFSTTAR1	0.214	0.165	0.119	0.106	0.184	7.44	0.98
IFSTTAR2	0.135	0.129	0.095	0.069	0.166	5.68	0.56
KAIST1	0.178	0.168	0.119	0.098	0.209	7.18	0.85
KAIST2	0.185	0.166	0.120	0.092	0.210	7.30	0.86
KyU1	0.071	0.064	0.047	0.034	0.084	2.63	0.13
KyU2	0.119	0.111	0.098	0.026	0.155	5.72	0.50
KyU3	0.143	0.133	0.116	0.033	0.185	6.74	0.72
NCU1	0.292	0.237	0.180	0.114	0.291	8.93	1.73
NCU2	0.224	0.202	0.151	0.101	0.247	7.43	1.20
NCU3	0.217	0.176	0.125	0.102	0.205	5.84	0.83
RPI1	0.150	0.146	0.135	0.021	0.221	7.02	0.82
RPI2	0.144	0.148	0.106	0.085	0.208	6.67	0.74
RPI3	0.170	0.162	0.144	0.036	0.233	7.25	0.92
UCD1	0.165	0.149	0.119	0.060	0.197	6.28	0.64
UCD2	0.339	0.210	0.149	0.122	0.249	8.25	1.13
UCD3	0.192	0.183	0.134	0.099	0.228	7.31	0.90
ZJU1	0.167	0.134	0.094	0.080	0.151	5.12	0.49
ZJU2	0.191	0.148	0.099	0.098	0.160	5.33	0.54
ZJU3	0.135	0.111	0.078	0.065	0.126	4.33	0.33
Average	0.181	0.158	0.120	0.077	0.201	6.791	0.859

cycles of the motion produced by the Ehime shaker are lower frequency than 1 Hz; this is a nuance of their mechanical shaker. The long period components did not much affect the PGA but did affect the cumulative absolute velocity and Arias intensity; Ehime motions were just below the median in terms of PGA_{eff}, but well above the median in terms of CAV_5 and I_a. From the highlighting in Table 4.2b, it is apparent that in most cases the intensity measures are highly correlated to each other; two apparent exceptions include the aforementioned effect of low-frequency components for the Ehime motions and weak correlation between PGA_{HF} to the intensity measures other than PGA.

Table 4.2c Performance measures for each of the experiments during the first destructive motion

Test ID	Integrated pos. rel. vel.	Peak dyn. rel. disp.	depth of liq., zliq	Duration of lique-faction at P4	Ux mean of all markers	Ux St. Dev. of all markers	Ux mean of 8 markers	Ux St. Dev. of 8 markers	Ux mean of 2 markers	Ux St. Dev. of 2 markers
	m	m	m	s	mm	mm	Mm	mm	mm	mm
CU1	5.80	0.066	3	58	359	77	403	56	440	57
CU2	5.52	0.056	3	28	359	96	428	65	490	42
Ehime1	5.42	0.047	2	0	--	--	--	--	--	--
Ehime2	7.18	0.061	1	0	89	48	103	39	100	28
Ehime3	9.63	0.055	0	0	56	37	65	37	60	28
IFSTTAR1	3.22	0.032	1	0	21	62	25	46	50	71
IFSTTAR2	5.66	--	2	31	272	160	297	227	438	53
KAIST1	3.05	0.037	1	2	1	3	0	4	2	2
KAIST2	4.58	0.063	1	20	0	57	0	37	0	28
KyU1	0.20	0.001	0	0	64	216	117	283	377	283
KyU2	4.61	0.040	3	20	108	44	141	43	150	61
KyU3	4.84	0.044	1	12	12	110	11	62	0	63
NCU1	8.73	0.113	2	13	197	70	248	40	287	1
NCU2	6.64	0.079	1	11	188	83	239	48	256	0
NCU3	4.61	0.054	2	14	233	79	270	59	279	56
RPI1	5.28	0.045	2	16	--	--	101	25	94	11
RPI2	5.73	0.061	2	14	--	--	128	22	134	12
RPI3	7.16	0.072	2	32	--	--	123	18	126	10
UCD1	0.63	0.004	0	0	12	30	0	28	0	28
UCD2	4.48	0.047	2	25	109	48	131	25	125	9
UCD3	5.54	0.051	2	19	116	80	134	35	160	3
ZJU1	4.39	0.035	1	18	133	56	150	53	135	21
ZJU2	5.41	0.046	1	25	221	86	283	33	263	53
ZJU3	0.40	0.002	0	0	29	42	26	16	30	21

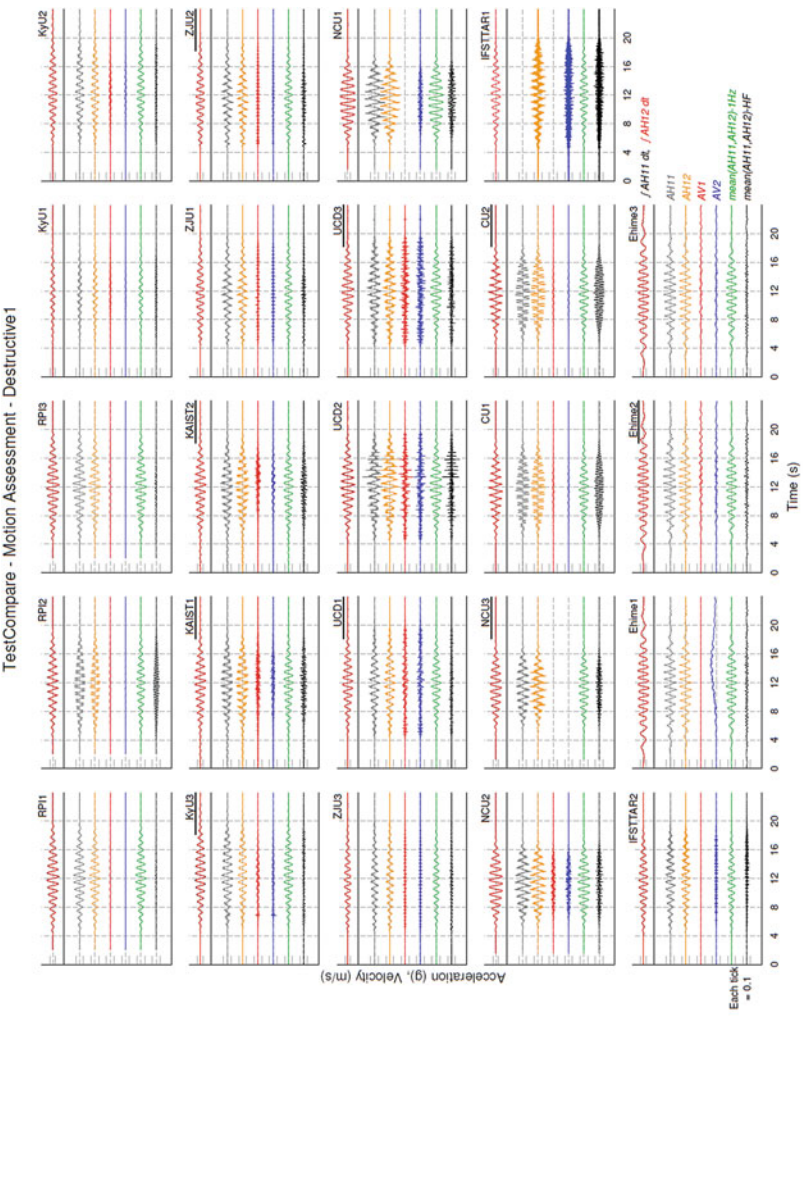

Fig. 4.5 Velocity time series data, horizontal accelerations, vertical accelerations, 1 Hz component, and high-frequency component of horizontal base motion

4.4 Acceleration Response of Soil Layers in First Destructive Motion

To allow for qualitative comparison of the acceleration response of the models, Fig. 4.6 presents time series data for the base horizontal acceleration in the soil. From top to bottom, each subplot shows AH4, AH3, AH2, AH1, and the base input motion presented in the same sequence as their physical location defined in Fig. 4.1.

Three of the experiments (KyU1, ZJU3, and UCD1) show almost uniform acceleration behavior—in other words, the models behaved like a rigid body—a clear indication that liquefaction did not occur in these experiments. All of the other experiments showed significant evidence of nonlinear behavior and evidence of liquefaction. The sharp downward spikes, most significant in AH3 and AH4, we call "dilation spikes" because they are caused by the sudden increase in effective stress and hence increase in stiffness associated with negative pore water pressures produced by the tendency of the sand to dilate in response to the imposition of large shear strains. The spikes are larger in the downward direction because this corresponds to shearing in the downslope direction; strains tend to accumulate in the downslope direction.

Some aspects of the recorded data are obviously influenced by faulty instrumentation. For example, the data from AH3 and AH4 in UCD1 show almost uniform behavior, similar to the base acceleration, indicating very little deformation of the soil; therefore, it is clear that the offset seen in AH1 and to a lesser extent AH2 are anomalous and probably due to an instrumentation issue. AH1 is not reported for UCD3, and AH1 is not reported for IFSTTAR2. AH1 appears to be nonfunctional (flat) in CU1.

Based upon the response recorded by the upper accelerometers (AH3 and AH4), CU1 shows the most severe isolation of the ground surface motion associated with liquefaction; towards the end of the earthquake record, the surface motion is almost flat. Other surface records that show severe spikes or isolation are Kaist2, ZJU2, NCU1, NCU2, NCU3, CU2, IFSTTAR2, and Ehime1. Consistent with this, all of these events also produced permanent displacements larger than 250 mm (see Table 4.2c).

4.5 Displacement Response of the Soil Layers in First Destructive Motion

It is difficult to directly measure the potentially large multidirectional deformations of submerged slopes by conventional contact sensors. A reliable alternative approach for measuring permanent displacements is by surveying the location of the surface markers before and after liquefaction as described in the specifications for LEAP-UCD-2017 (Kutter et al. 2019). The surveys may be accomplished by direct measurement using rulers and calipers or by photography or surface scanners. High-

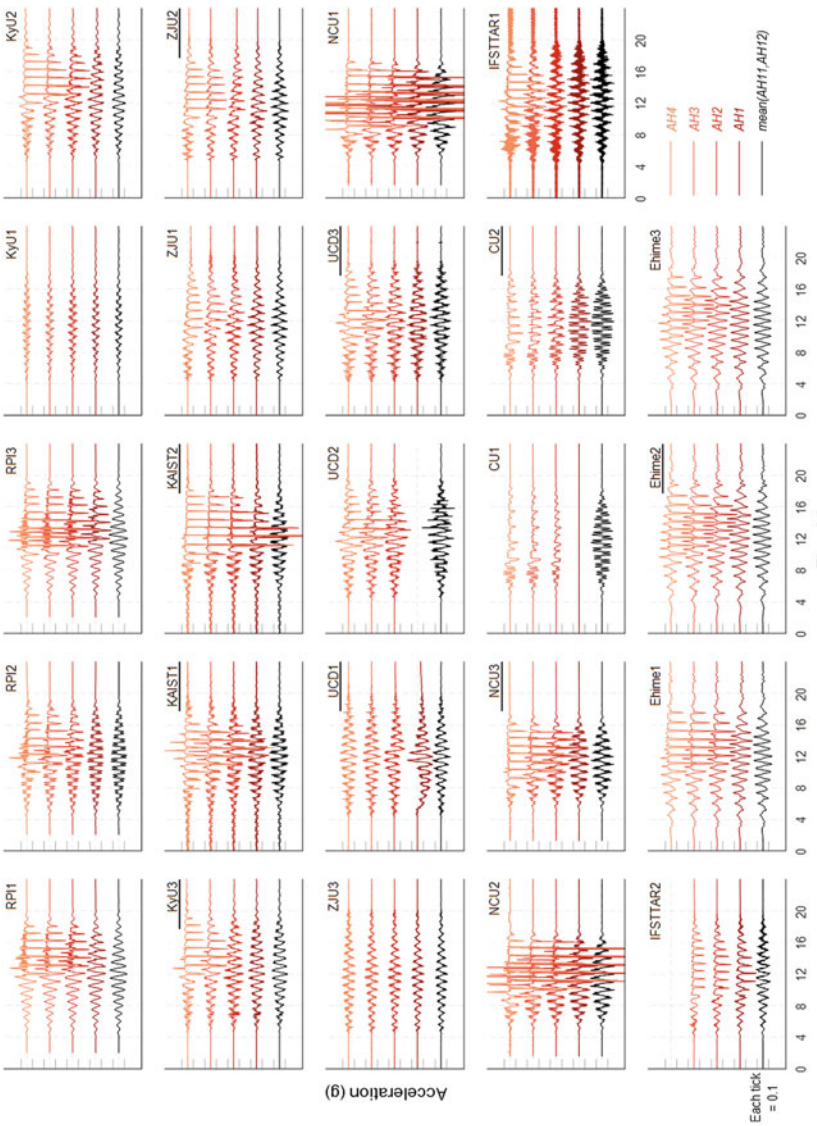

Fig. 4.6 Acceleration response in the soil layers

speed photography at some sites allowed not only the determination of the residual deformations but also dynamic measurement of displacements during shaking. Dynamic displacements from photography are presented in the papers submitted by the experimenters from each site.

Vectors of the horizontal component of the displacement from before-and-after surveys of the surface markers are shown in Fig. 4.7. The data source for these plots is available in a spreadsheet document that is archived in the LEAP-UCD-2017 data archive in DesignSafe (Kutter et al. 2018b). The length of the displacement vectors is magnified by a factor of 6 compared to the geometry of the model. According to the specifications, markers were to be placed in a 6 × 3 grid across the surface. One site (RPI) reported displacement data from high-speed camera measurements of a different pattern of surface markers, so the patterns of the vectors are different. The data from KyU1 indicate substantial out-of-plane displacements that might be explained by a systematic error. Figure 4.7 also shows the locations of the model boundaries. All of the models were 20 m long in prototype scale, but some of the models (Ehime and Kyoto) were narrower than the others. In general, the displacements tended to be greatest near the middle of the container and tapered off near the ends of the container. (The ends of the container are defined by X-coordinate = ±10 m.) Settlements tended to be large on the upslope (left side of each subfigure) and smaller or negative on the downslope end of the sample container.

The X-components and Z-components of the displacement vectors are shown in contour plots in Figs. 4.8 and 4.9, respectively. From the contour plots, it is apparent that the experiments covered a wide range of displacements.

Although the dynamic component of the surface displacement cannot be determined from the before and after surface marker displacements, the dynamic component of the relative displacement, shown by the lighter lines in Fig. 4.10, was obtained by subtracting acceleration at AH4 from the acceleration at the base of the container and then double integrating with respect to time. Following each integration, a 0.2 Hz (prototype scale) high-pass filter was applied to remove drift error due to integration.

Also in Fig. 4.10, the curve labeled "scaled IPRV" represents a ramp, the shape of which is determined by the "integrated positive relative velocity" defined by Kutter et al. (2017):

$$\text{IPRV} = \int_0^\infty \chi[v_{\text{rel}}(t)]dt$$
$$\text{where } \chi = \left\{ \begin{array}{ll} 0 & \text{if } v_{\text{rel}}(t) < 0 \\ 1 & \text{if } v_{\text{rel}}(t) > 0 \end{array} \right\} \tag{4.3}$$

where v_{rel} is the dynamic component of the relative velocity from single integration of the difference between AH4 and the base acceleration. This function produces a reasonably shaped ramp that should be representative of the accumulation of the permanent displacements. The IPRV ramp function is then scaled to make it agree with the displacement determined from surface marker surveys. The time series

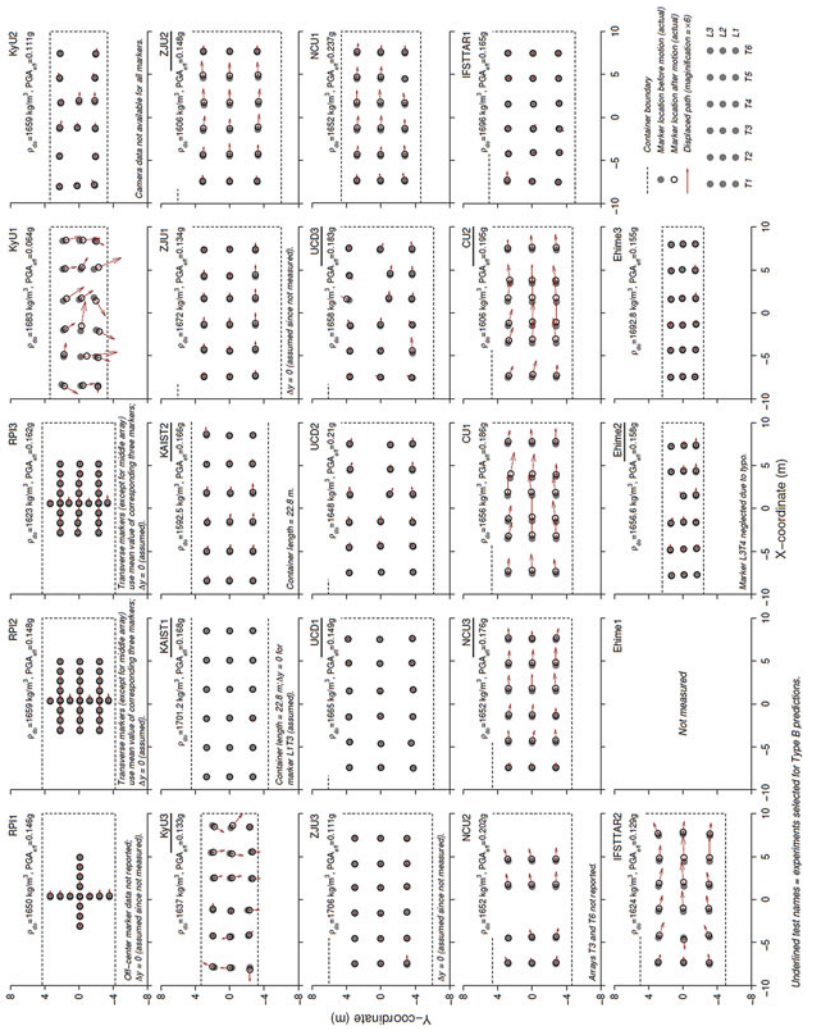

Fig. 4.7 Horizontal component of the displacement vectors superimposed on plan view of the surface markers on the top of the sand

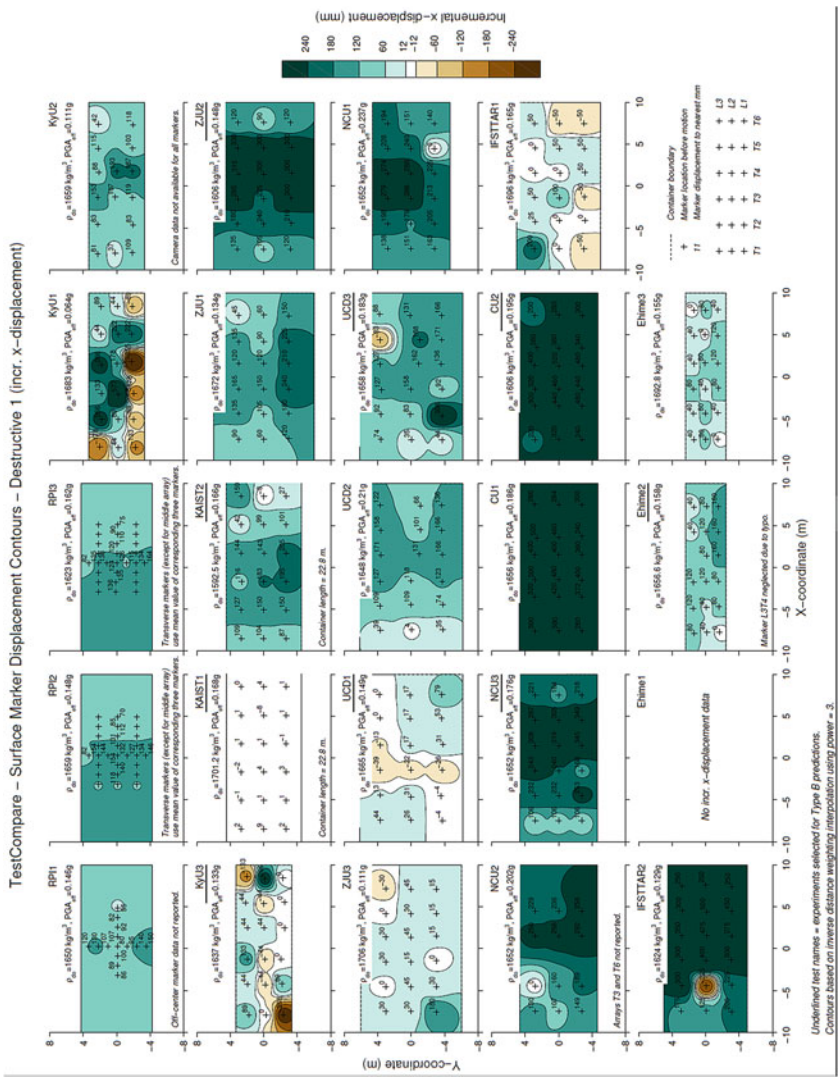

Fig. 4.8 Contours of X-component of the surface marker displacement

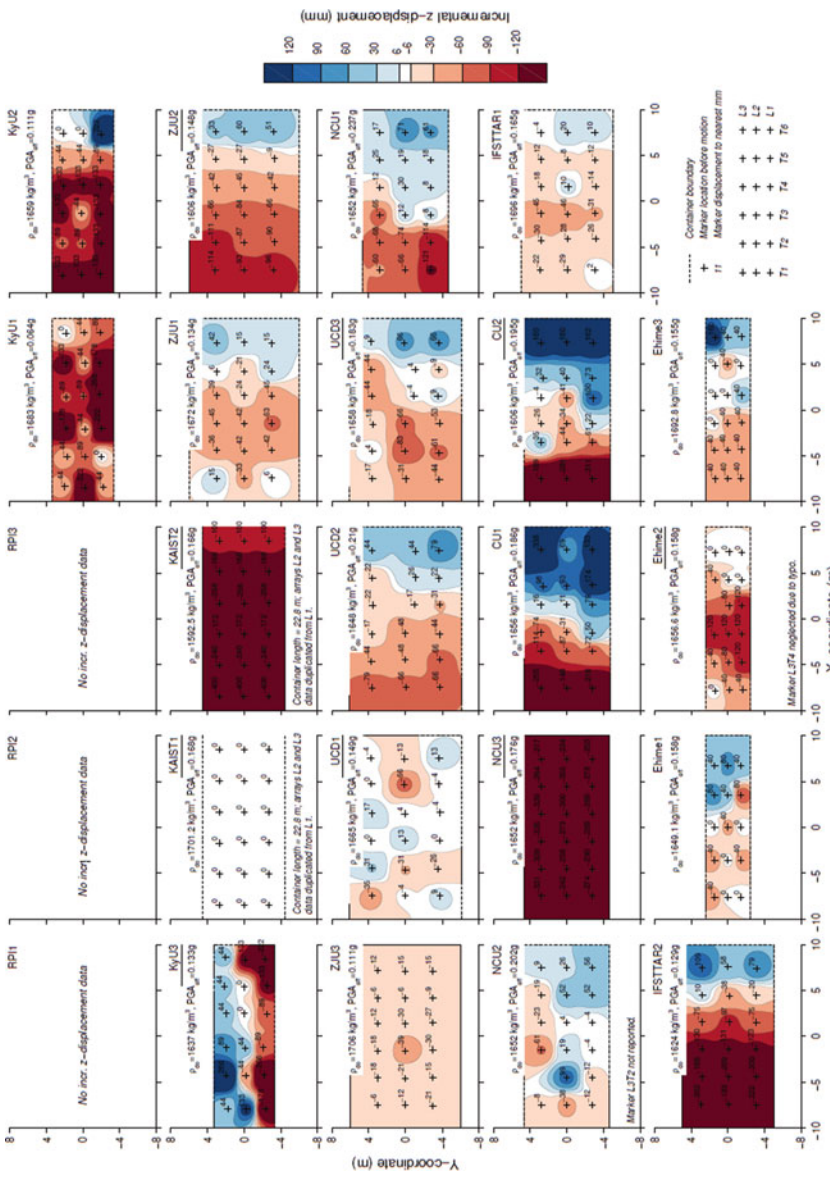

Fig. 4.9 Contours of Z-component of the surface marker displacement

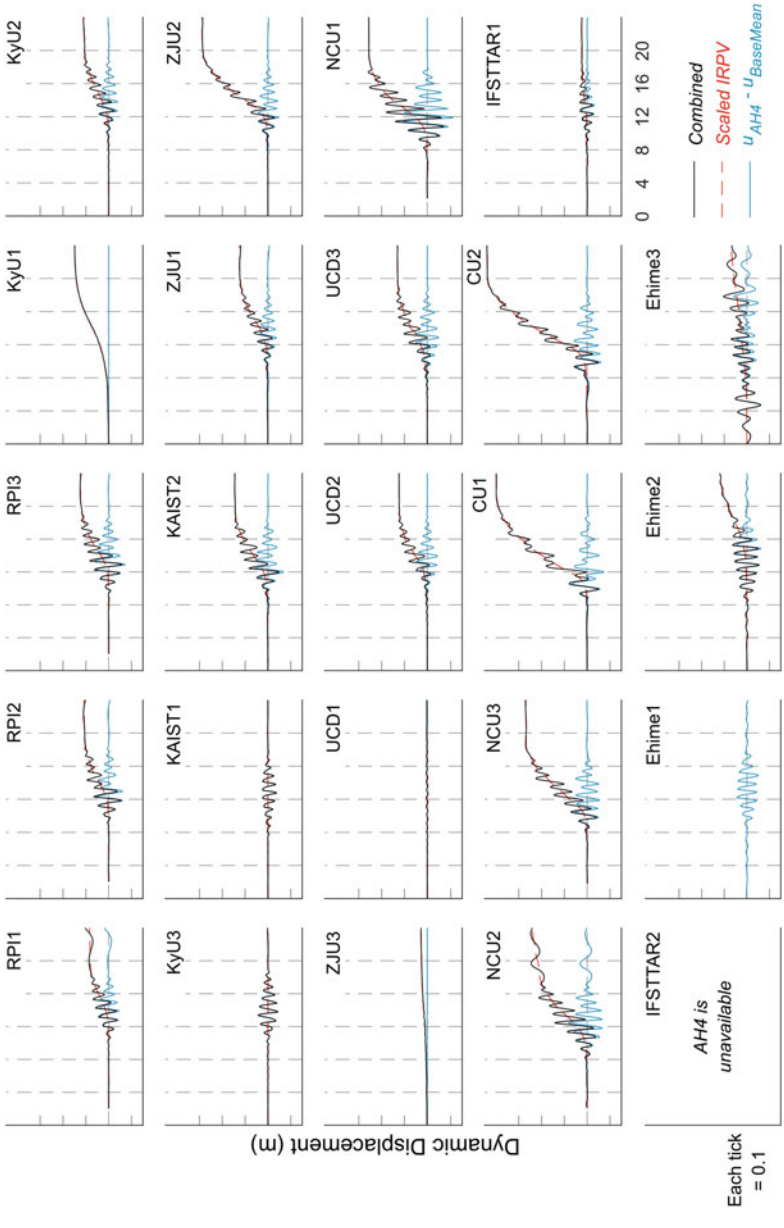

Fig. 4.10 Dynamic component of the relative displacement $u_{AH4} - u_{BaseMean}$, the scaled integrated positive relative velocity, and the sum of the IPRV and the dynamic component of relative displacement

labeled "combined" is obtained by adding the scaled IPRV ramp to the dynamic component of the displacement. Carey et al. (2018a, 2019b) independently determined the displacement of the surface markers as a function of time using the high-speed cameras and demonstrated that superposition of the dynamic displacements from accelerometers on the IPRV ramp produces a reasonable approximation of the displacement time series. From Fig. 4.10, the cyclic components of the displacements are negligible for tests UCD1, ZJU3, and KyU1, as would be expected considering that these models did not liquefy. The fact that KyU1 showed a permanent displacement but no cyclic displacement may be explained by the earlier observation that there may have been a systematic error in the surface marker measurement for KyU1. The cyclic displacements were the largest for test NCU1. The IPRV and the amplitude of the cyclic component of relative displacements are considered to be meaningful and reliably quantified measures of the performance of the models that would not be affected by errors in surface marker measurements; therefore, these performance measures are listed in Table 4.2c.

4.6 Pore Pressure Response of Soil Layers in First Destructive Motion

Figure 4.11 compares the pore water pressure responses from the first destructive motions for the central array for all of the experiments. Note that the time scale is broken, with compressed time scale in the latter part of the graph to show the dissipation of pore pressures. The top four traces in each subplot show results from P4, P3, P2, and P1 (depth $\approx$ 1, 2, 3, and 4 m prototype scale; initial effective overburden stress $\approx$ 10, 20, 30, and 40 kPa, respectively). The buoyant unit weight of the saturated sand is approximately 10 kN/m^3. The tick marks on the side of each subplot correspond to 10 kPa. The last trace in each subplot shows results from P10, a sensor in the bottom corner of the containers. It is interesting to note that, especially near the beginning of shaking, the cyclic pore pressures at P10 tend to be greater than those in the central array, possibly in response to the cyclic total stress oscillations near the wall.

Consistent with the small cyclic relative displacements in UCD1, ZJU3, and KyU1 apparent from the accelerometer arrays, these three tests showed relatively small pore pressures throughout the layer. In UCD1 and ZJU3, the pore pressure approached the overburden of 10 kPa at P4 during shaking, but only at the peaks of the cycles, and dissipation began during shaking. For all of the other models, the pore pressures appeared to reach the effective overburden stress. The extent of liquefaction could be determined by pore pressure ratios, but small errors in the depth of the sensors could make the difference between pore pressure ratios of 100% and 90%, which is significant.

In search of a more robust measure of the extent of liquefaction, we systematically measured the duration of time over which the high pore pressures were

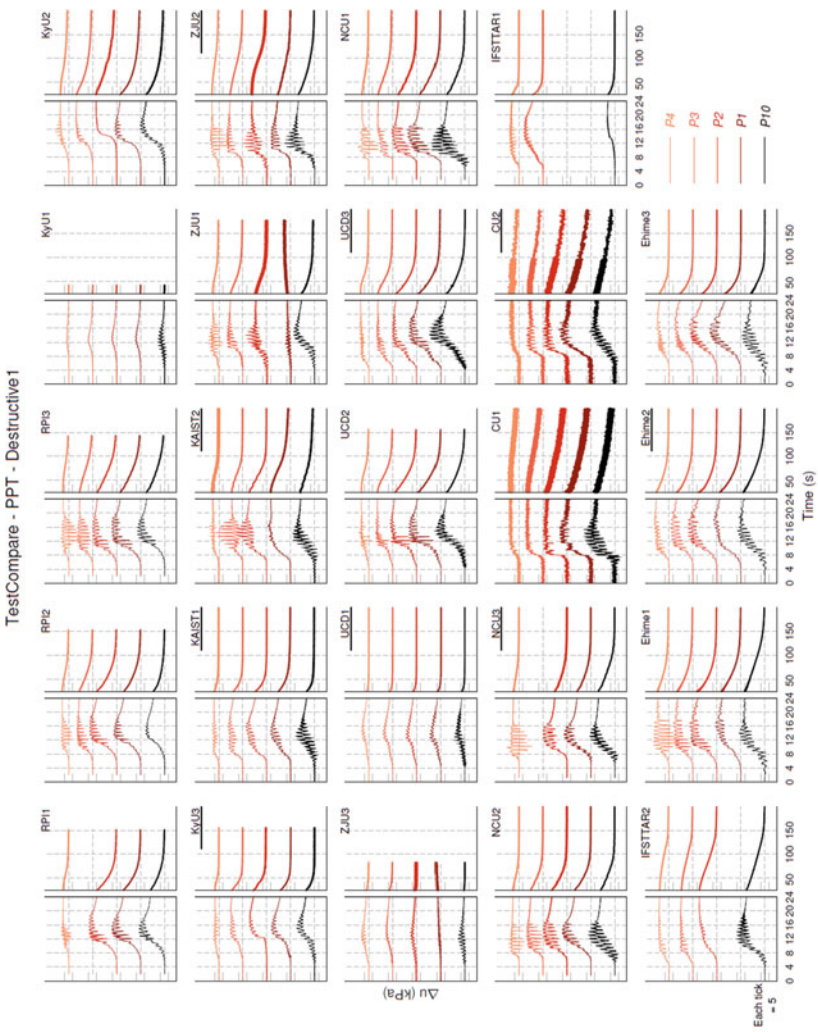

Fig. 4.11 Pore pressure time series from the central array, first destructive ground motion

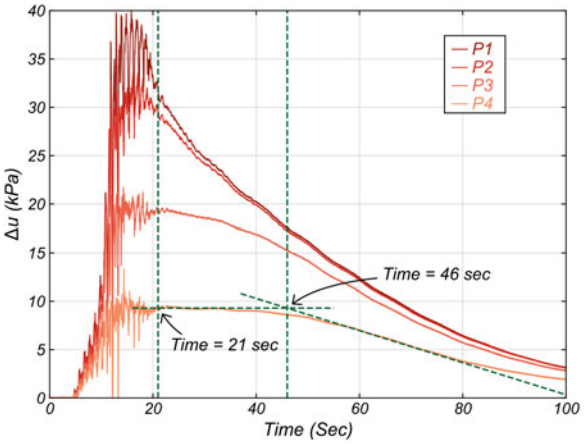

Fig. 4.12 Pore pressures in the central array for UCD2 to illustrate the method of estimating the duration of liquefaction at P4. The second vertical line is drawn through the intersection of a near horizontal line through the time of sustained high pore pressure and a sloping line through the inflection of the dissipation curve. The end of shaking is indicated by the first vertical line and the beginning of dissipation is indicated by the second vertical line

sustained at sensor P4 after shaking stops as illustrated in Fig. 4.12. Sustained high pore pressures at P4 is an indication that large hydraulic gradients are uniform around that point. If hydraulic gradients are uniform at P4, then the upward flow toward P4 will be equal to the upward flow away from P4, and the pore pressure would be constant. The duration of sustained pore pressures at P4 is indicative of the duration of large exit gradients at the soil surface; hence, the duration of sustained pore pressures will be an indicator of the volumetric strains caused by the shaking event. If, for example, the duration of large exit gradients (approximately, $i \sim i_{crit} \sim 1$) is 20s in prototype scale, and the permeability of the sand is 1.5×10^{-4} m/s (El Ghoraiby et al. 2017), then the volume of water expelled would be (20 s) $(1.5 \times 10^{-4}$ m/s) $= 3$ mm in prototype scale. After some time a break in the dissipation curve is apparent in Fig. 4.12. Such a construction was repeated for each of the first shaking events for all 24 experiments. The duration of sustained pore pressures determined by this method is summarized in Table 4.2c.

Also apparent in Figs. 4.11 and 4.12 are large spikes of negative pore pressure that appear in many traces after liquefaction develops; these negative pore pressures are attributed to dilatancy and have been observed in many laboratory element tests as well as centrifuge tests in the past. As expected, these spikes of negative pore pressure increase the effective stress and stiffen the sand and tend to be aligned with corresponding spikes of ground acceleration. The large dilatancy spikes correspond to the arresting of downslope displacements. In some sensors for some experiments, positive spikes of pore pressure are also apparent; because effective stress in sand cannot be negative, the only mechanism for which pore pressures in a soil layer could be greater than the initial total vertical stress is if the total stress is momentarily

increased by dynamic vertical accelerations. Anomalous positive pore pressures might also be recorded by sensors due to local pushing or pulling on sensor cables or other soil-sensor interactions.

4.7 Correlations Between Displacement, D_r, and IMs

Figure 4.13, reproduced from Kutter et al. (2018a), shows two views of 3D plots of correlations between the observed displacement from the average of the two central surface markers (Ux2 in units of mm) as a function of relative density from cone penetration resistance ($D_r(q_c(2\text{ m}))$) and PGA_{eff} for 16 of the 19 tests that provided this information. All of the available data for the 24 tests used as a data source are listed in Tables 4.2a, 4.2b, and 4.2c. In addition, the data will also be available in a spreadsheet document available in the LEAP-UCD-2017 data archive in DesignSafe (https://www.designsafe-ci.org). Three of the 19 tests were excluded from the correlations because they were thought to be "outliers." With the outliers excluded, the coefficient of correlation $R^2 = 0.846$, indicating that 84.6% of the variation between these results could be explained by the two variables PGA_{eff} and $D_r(q_c(2\text{ m}))$. Kutter et al. (2018a) also presented surface fits through using the same fitting function but for all 19 points without excluding outliers. Inclusion of the outliers reduced the correlation coefficient considerably to $R^2 = 0.578$.

The shape of the surface used to perform the regression was loosely based on curves presented by Yoshimine et al. (2006). Idriss and Boulanger (2008) approximated the Yoshimine et al. curves by:

$$\gamma_{max} = 0.035\left(2 - FS_{liq}\right)\frac{1 - F_\alpha}{FS_{liq} - F_\alpha} \tag{4.4}$$

where FS_{liq} = CRR/CSR is the factor of safety with respect to triggering of liquefaction and F_α is a function of relative density. Note that Eq. 4.4 is not applicable if FS_{liq} is greater than 2 and would return a strain potential, γ_{max}, of zero for $FS_{liq} = 2$. The curve fit equation used for displacement for this study was:

$$Ux = b_2\left\langle b_1 - \frac{(D_r - 0.125)^{n3} + 0.05}{1.3\frac{a_{max}}{g}}\right\rangle^{n1}\left(\frac{a_{max}}{g}\right)^{n2}(1 - D_r)^{n4} \tag{4.5}$$

where the second term inside the Macauley brackets $\langle\rangle$ is meant to be analogous to FS_{liq} and the b1 term corresponds to the constant, 2, in Eq. 4.4. Note that $\langle x\rangle = x$ if $x > 0$; $\langle x\rangle = 0$ if $x < 0$. However, for the present study, coefficients b_1, b_2, n1, n2, n3, and n4 are determined by nonlinear regression. Inclusion of the term in Macauley brackets, with the restriction that $0.125 < D_r < 1$, produces a smooth function and prevents this function from producing not-physically realistic uphill residual displacements. As an example, the curve fit parameters determined using a nonlinear

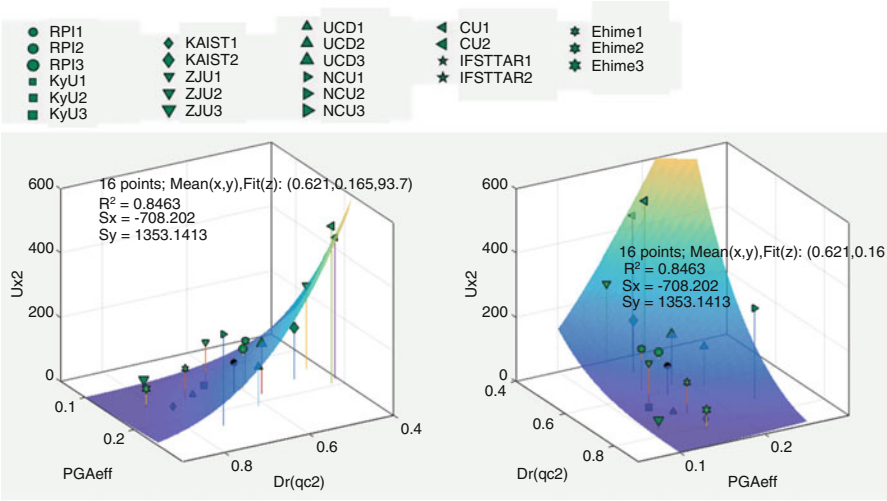

Fig. 4.13 Two views of the correlation between the median displacement of the two central surface markers (U×2 mm, prototype scale), PGA_{eff} (g), and relative density determined from q_c(2 m). This result is for Case 1/6 in Table 4.3 and was also presented by Kutter et al. (2018a). An excellent coefficient of correlation $R^2 = 0.846$ is obtained

regression algorithm in Matlab that produced the surface plotted in Fig. 4.13 are $b_1 = 12$, $b_2 = 0.0456$, n1 = 4.57, n2 = 1.157, n3 = 1, and n4 = 2.

The first four cases summarized in Table 4.3 are reproduced from Kutter et al. (2018a) using the six-parameter fitting equation (Eq. 4.5). The table summarizes the results of the surface fitting discussed in the previous paragraphs and in addition the surface fitting results of the analysis using D_r(Mass & Vol.) in place of D_r(q_c(2 m)) in case 3 and using PGA instead of PGA_{eff} as a shaking intensity measure in case 4. The R^2 values summarized in Table 4.3 suggest that PGA_{eff} is a better indicator of shaking intensity than PGA and that D_r(q_c(2 m)) is a better indicator of liquefaction resistance than is D_r(Mass & Vol.) for the present dataset. The mean density and shaking intensity measure (IM) of the data points analyzed are summarized in the last column of Table 4.3 along with the evaluation of the surface function at these means.

Case 5 shows a later analysis done after one more data point from test IFSTTAR2 became available. IFSTTAR2 produced relatively large deformations compared to the rest of the dataset; hence the R^2 value decreased from 0.846 to 0.718 by including this one point. Note however that evaluation of the curve fit at the median was not affected much by this point, and the computed sensitivities were not drastically changed by the addition of this data point. For the five cases summarized, the mean D_r varied from 0.61 to 0.65; the mean IM varied from 0.161 to 0.185 g, and the surface fit at the median point varied from 94 to 154 mm. The table also summarizes the sensitivity of the displacement to variation of the D_r and IM. The sensitivity of displacement to D_r(q_c(2 m)) varied by a factor of 1.29 (between −645 and −829 mm), and the sensitivity to PGA_{eff} varied by a factor of 1.57 (between 1356 and 2125 mm/g) for the various cases. While there is

Table 4.3 Results of nonlinear regression between displacement, relative density, and motion intensity for the first destructive motion in LEAP-UCD-2017

Case/ (# pars)	Motion intensity measure (IM) (g)	Basis to determine D_r	Data points used/ excluded outliers	Correlation coef. R^2	Sensitivity to D_r at mean (mm)	Sensitivity to IM at mean (mm/g)	Mean D_r, mean IM, and evaluation of curve fit at mean (1, g, mm)
1/6	PGA_{eff}	q_c(2 m)	16/3	0.846	−708	1356	0.62, 0.165, 94
2/6	PGA_{eff}	q_c(2 m)	19/0	0.578	−645	2125	0.62, 0.161, 131
3/6	PGA_{eff}	Mass & Vol.	19/4	0.603	−492	1804	0.65, 0.166, 131
4/6	PGA	q_c(2 m)	19/0	0.485	−829	611	0.62, 0.185, 154
5/6	PGA_{eff}	q_c(2 m)	17/3	0.718	−568	2339	0.60, 0.163, 106
6/4	PGA_{eff}	q_c(2 m)	17/3	0.756	−598	2681	0.60, 0.163, 106

variability in the sensitivities obtained by these methods, it is believed that the sensitivities are consistent enough to claim that the results are statistically significant. The compilation of sufficient data from centrifuge tests to enable quantification of the mean, sensitivities, and correlation is unprecedented.

Figure 4.14 (lower left) shows the same contour plot from Fig. 4.14 (upper left), with displacements normalized by the 4 m-layer thickness to produce an average shear strain using green dashed lines. Superimposed on Fig. 4.14 are contours from Eqs. 89–92 of Idriss and Boulanger (2008); their shear strain equations are based on a curve fit to cyclic stress-controlled triaxial tests reported by Yoshimine et al. (2006). Their equations relate cyclic stress ratio and relative density to shear strains. To map their CSR values onto the PGA_{eff} vertical axis, the CSR values were divided by 1.3 for reasons explained below.

To revisit the assumptions of the nonlinear regression, the regression model was simplified from the six-parameter regression model (Eq. 4.5), to a four-parameter regression model (Eq. 4.6), and surprisingly, a better coefficient of correlation was obtained: $R^2 = 0.753$. The result (b1 = 5.985, b2 = 1.416, n1 = 4, n3 = 0.705) is plotted in Fig. 4.15. The values of the exponents n1 and n2 were arbitrarily limited to not exceed 4.0, and the converged value of n1 = 4 was fixed by this constraint.

$$Ux = b_2 \left\langle b_1 - \frac{(D_r - 0.125)^{n3} + 0.05}{1.3\frac{a_{max}}{g}} \right\rangle^{n1} \tag{4.6}$$

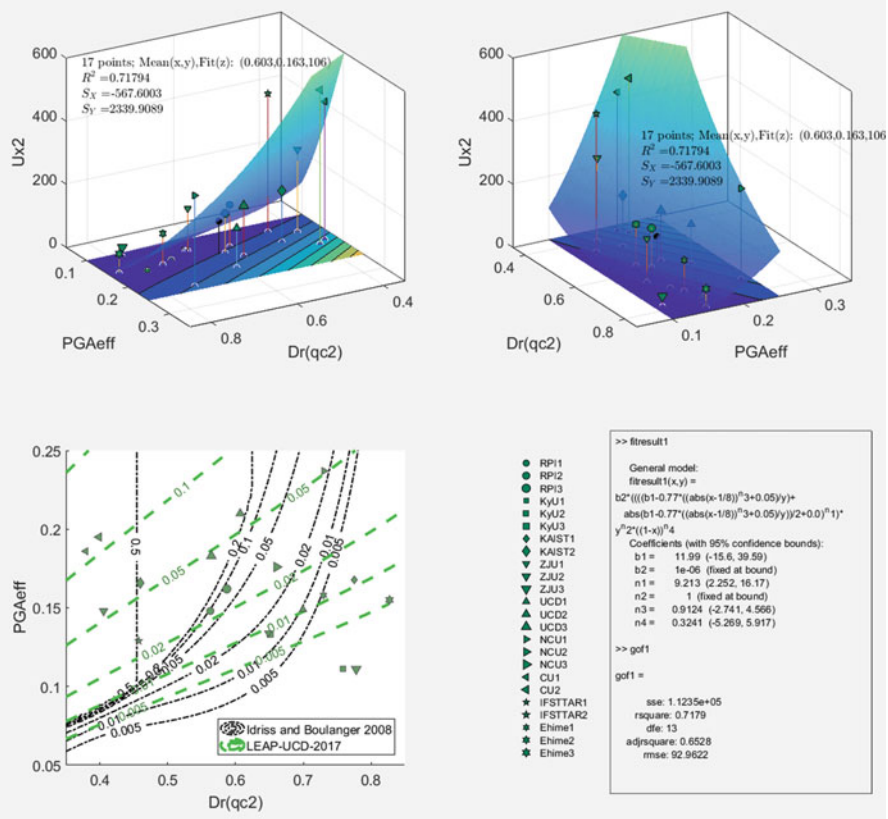

Fig. 4.14 (**a**) Reevaluation of the six-parameter model surface fit after adding a new data point (IFSTTAR2) to the same dataset as used for Fig. 4.13. R^2 is reduced to 0.718. This result is for Case 5/6 in Table 4.3. The contour plot on the bottom left of the figure maps the same fitted surface displacement divided by the soil layer thickness (4000 mm) to convert the displacement to an average soil strain. These strains from the LEAP-UCD-2017 data are compared to a contour plot of Idriss and Boulanger (2008) (see Eq. 4.4)

In statistics, the "adjusted R^2" value is meant to compensate for the tendency for R^2 to decrease as additional parameters are introduced to the model. The "adjusted R^2" = 0.653 for the six-parameter model illustrated in Fig. 4.14. For the four-parameter model, the "adjusted R^2" = 0.722 is superior to that for the six-parameter model. It is interesting but certainly possible that introduction of additional parameters being fit by a nonlinear regression algorithm selected in Matlab could result in convergence to a different local minimum. Despite the simplification of the model, the resulting contours from the four-parameter model (Fig. 4.15) bear major resemblance to contours from the six-parameter model (Fig. 4.15). The results from regression to the same 17 data points for the four-parameter model are summarized as Case 6/4 in Table 4.3.

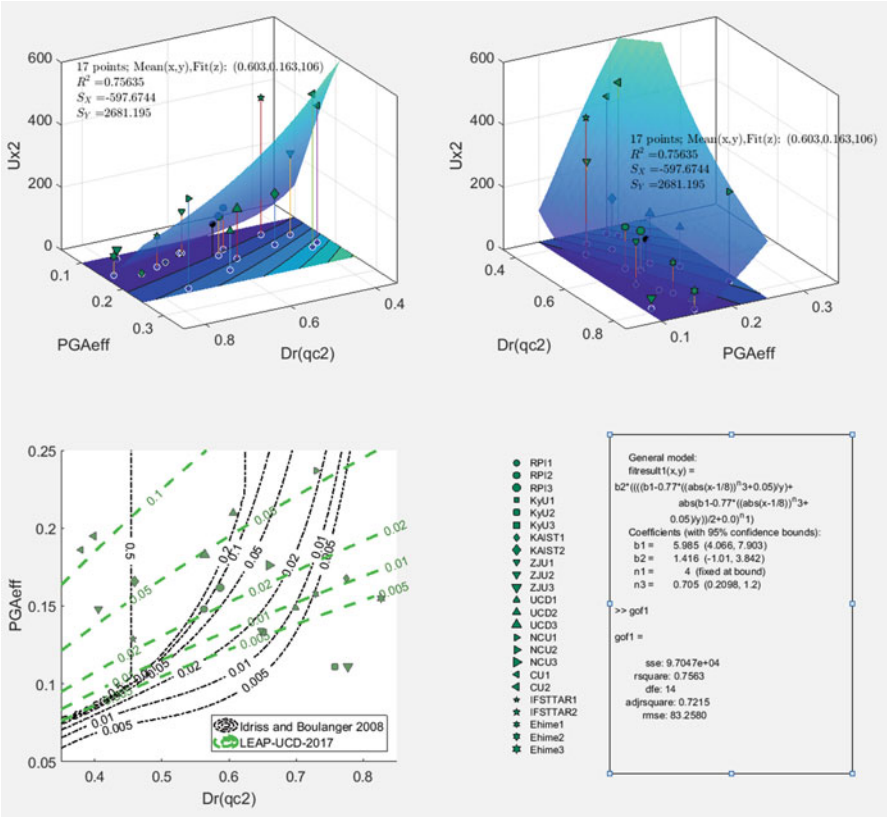

Fig. 4.15 Results of linear regression using the simplified four-parameter model; $R^2 = 0.756$. This result is for Case 6/4 in Table 4.3. (**b**) The contour plot on the bottom left of the figure maps the same fitted surface displacement divided by the soil layer thickness (4000 mm) to convert the displacement to an average soil strain. These strains from the LEAP-UCD-2017 data are compared to a contour plot of Idriss and Boulanger (2008) (see Eq. 4.4)

4.7.1 Rationale for Scaling Between PGA and CSR for Simplified Procedure

According to the Idriss and Boulanger (2008) simplified procedure, the cyclic stress ratio scaled to a magnitude 7.5 earthquake with a vertical effective stress of 1 atm (101 kPa) is given by:

$$\mathrm{CSR}_{M=7.5,\ \sigma'_{vc}=1} = 0.65(\gamma/\gamma')(\mathrm{PGA}/g)(r_d)(1/\mathrm{MSF})(1/K_\sigma)(1/K_\alpha) \qquad (4.7)$$

The ratio of total to buoyant densities of the soil $\gamma/\gamma' \approx 2$, and the depth reduction factor, r_d, is very close to 1.0 for a 4 m-deep deposit. According to Idriss and

Boulanger (2008, Fig. 65), for a static stress ratio of 0.09 (which corresponds to a 5-degree slope angle), the static shear stress correction factor, K_α, may vary between about 0.8 for looser sand and 1.2 for the denser sand; for the purposes of this paper, it is assumed that $K_\alpha = 1$. From a cycle counting procedure, it was determined that the prescribed ramped sine wave LEAP motion corresponds to an earthquake of magnitude $M = 7.7$ to 7.9; the corresponding magnitude scaling factor, MSF, would be approximately 0.9. The overburden stress correction factor, K_σ, would be greater than 1 because the confining pressures at mid-depth of the liquefiable soil are only on the order of 20 kPa. According to Idriss and Boulanger (2008), the correction factor depends on density as well as confining stress, and it is capped at $K_\sigma \leq 1.1$. Assuming that the cap controls, the effect of $K_\sigma \approx 1.1$ would effectively offset $MSF \approx 0.9$ in Eq. 4.7. Inserting the above-described constants into Eq. 4.7 and using $\mathrm{PGA_{eff}}$ in place of *PGA* provides $\mathrm{CSR}_{M=7.5,\ \sigma'_{vc}=1} \approx 1.3(\mathrm{PGA_{eff}})$.

4.8 Correlations Between Excess Pore Pressures, D_r, and IMs

As explained in Sect. 6, the duration of liquefaction near the top boundary of the sand (see Fig. 4.12) is explored as a potential robust measure of the extent of liquefaction in a centrifuge test. The durations of liquefaction at sensor P4 (1 m deep) are tabulated in Table 4.2c. The duration of liquefaction is plotted as a function of $D_r(q_c(2\ \mathrm{m}))$ and PGAeff in Fig. 4.16; panels (a) and (b) show two different views of the 3D plot, and (c) shows residuals between the fit and the data points. Twenty of the twenty-four centrifuge tests provided $q_c(2\ \mathrm{m})$. One of these 20 was considered to be an outlier and is excluded from Fig. 4.16. The coefficient of correlation for this regression was found to be $R^2 = 0.78$, indicating that 78% of the variation can be explained by the fitting function with the variables $\mathrm{PGA_{eff}}$ and $D_r(q_c(2\ \mathrm{m}))$. This is considered to be a clear indication that the LEAP centrifuge tests performed at different centrifuge facilities are very consistent from centrifuge to centrifuge. The thin dash-dot line in Fig. 4.16 shows the liquefaction triggering curve from Boulanger and Idriss based on the relative density at mid depth of the layer. The CRR (Cyclic Resistance Ratio) curves were scaled according to $\mathrm{CRR} = 1.3 \times \mathrm{PGA_{eff}}$ as explained in Sect. 7.1. The empirical triggering curve seems to be consistent with the LEAP-UCD-2017 data.

Figure 4.17 presents a similar set of plots, with R^2 reduced from 0.78 to 0.47 due to replacement of the density measure $D_r(q_c(2\ \mathrm{m}))$ by the density measure $D_r(\mathrm{rho})$. $D_r(\mathrm{rho})$ is determined from direct measurements of mass and volume, while $D_r(q_c(2\ \mathrm{m}))$ uses the density obtained by correlations with the cone penetration resistance at mid-depth. As was the case for the correlations to displacement, $D_r(q_c(2\ \mathrm{m}))$ produces a better correlation than relative density from mass and volume measurements. This is likely caused by cumulative errors in the direct measurement of mass and volume.

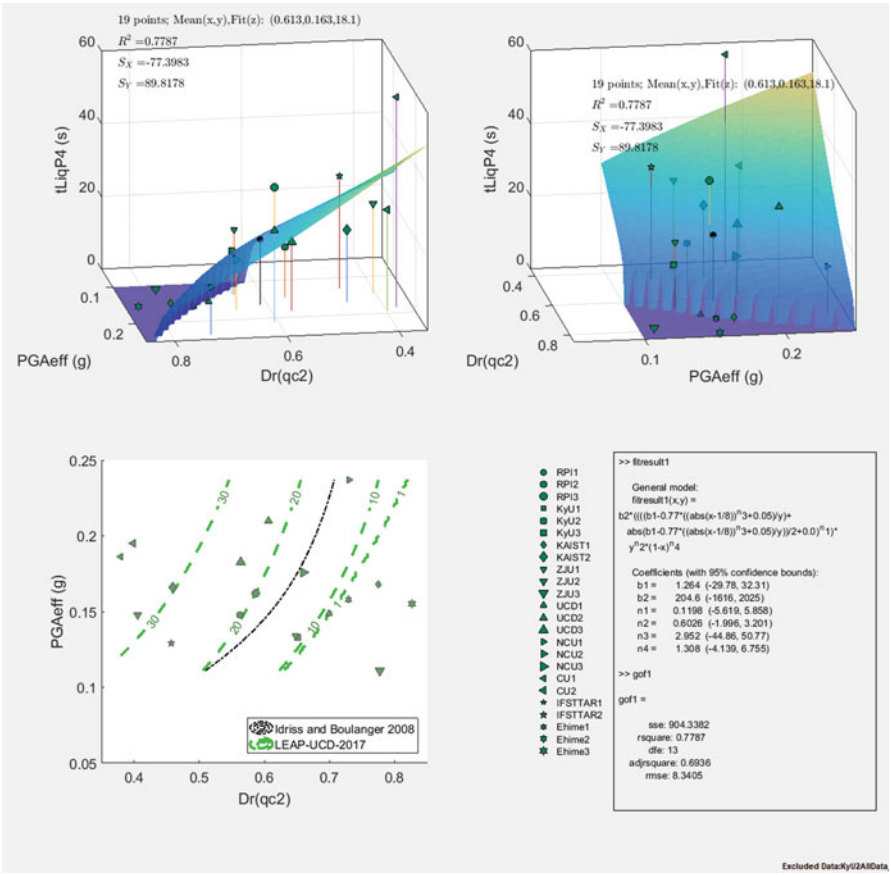

Fig. 4.16 Correlation between duration of liquefaction at P4, PGA_{eff}, and $D_r(q_c(2\text{ m}))$. 19 of 20 experiments with requisite data are plotted (one outlier was excluded), and $R^2 = 0.78$. Panels (**a**) and (**b**) show two views of the same surface fit to the data. Panel (**c**) shows a contour plot in green, overlaid on the Idriss and Boulanger (2008) triggering curve. The same six-parameter model was used (Eq. 4.5)

R^2 reduced slightly from 0.78 in Fig. 4.16 to 0.73 in Fig. 4.18 when CAV_5 is used in place of PGA_{eff} as the IM. As was concluded by Kutter et al. (2018a), the R^2 value is best when IM = PGA_{eff} and when relative density is based on the cone measurements. However, the correlation of the duration of liquefaction at P4 to CAV_5 is also very good.

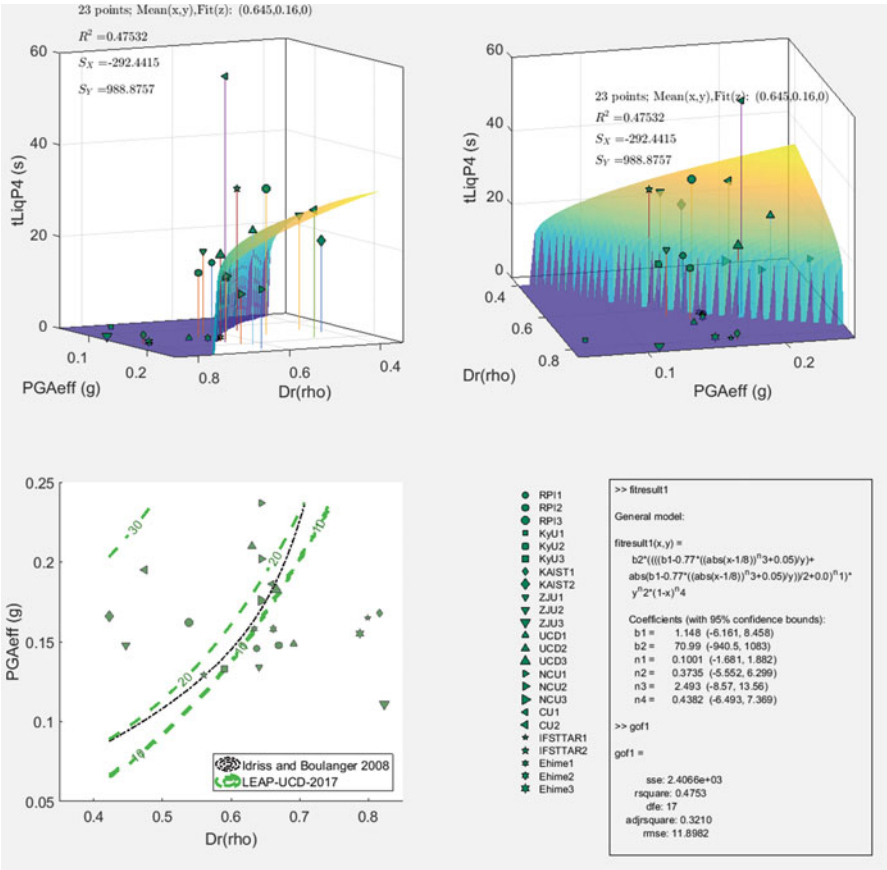

Fig. 4.17 Correlation between duration of liquefaction at P4, PGA_{eff}, and D_r(rho), based on measurements of mass and volume. 23 of 24 experiments with requisite data are plotted (one outlier was excluded), and $R^2 = 0.48$. Panels (**a**) and (**b**) show two views of the same surface fit to the data. Panel (**c**) shows a contour plot in green, overlaid on the Idriss and Boulanger (2008) triggering curve. The same six-parameter model was used (Eq. 4.5)

4.9 Correlations Between Peak Cyclic Displacements, D_r, and IMs

Another easily measurable quantity thought to be indicative of the extent of liquefaction is the magnitude of the average cyclic component of the shear strains in the soil layer. This quantity can be reliably computed as described by Kutter et al. (2017). Briefly, it is obtained by subtracting the accelerations of the base of the container (average of accelerometers AH11 and AH12) from the accelerations measured at the surface of the soil layer (accelerometer AH4) and then double

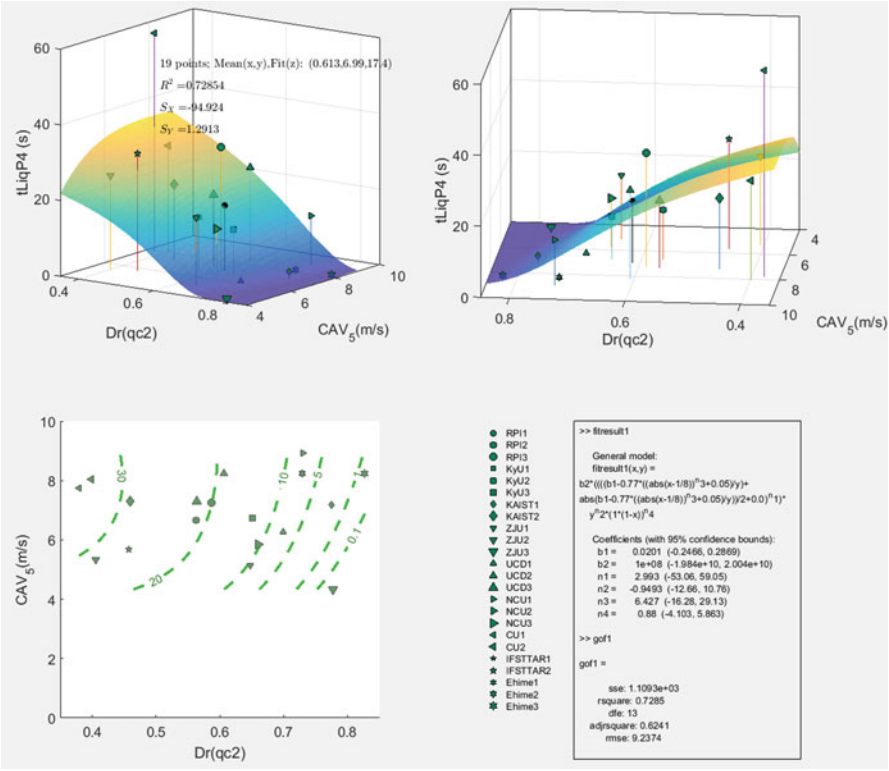

Fig. 4.18 Correlation between duration of liquefaction at P4, CAV5, and $D_r(q_c(2\text{ m}))$. 19 of 20 experiments with requisite data are plotted (one outlier was excluded), and $R^2 = 0.73$. Panel (**a**) shows a contour plot; panel (**b**) shows a side view of the function. The same six-parameter model was used (Eq. 4.5)

integrating to determine the displacement as a function of time. A high-pass filter (about 0.3 Hz prototype scale) is used to remove the low-frequency components of the accelerations before integrating to obtain velocities and displacements. The low-frequency components, often a result of small electrical drift in the signal, become large during integration and are not reliably measured by accelerometers. Unfortunately, the filtering of the low-frequency component also removes the evidence of permanent displacements on the acceleration signal. Nevertheless, the amplitude of the cyclic component (higher than 0.3 Hz prototype scale) is also indicative of softening due to liquefaction. Figure 4.10 showed the cyclic time series of the cyclic component of displacement as a function of time. The peak of the cyclic displacement time series is summarized in Table 4.2c.

Figure 4.19 shows the relationship between the relative density, effective PGA, and the peak cyclic component of the relative displacement. The curve fit almost produced a step function; relative displacements are negligible if liquefaction is not

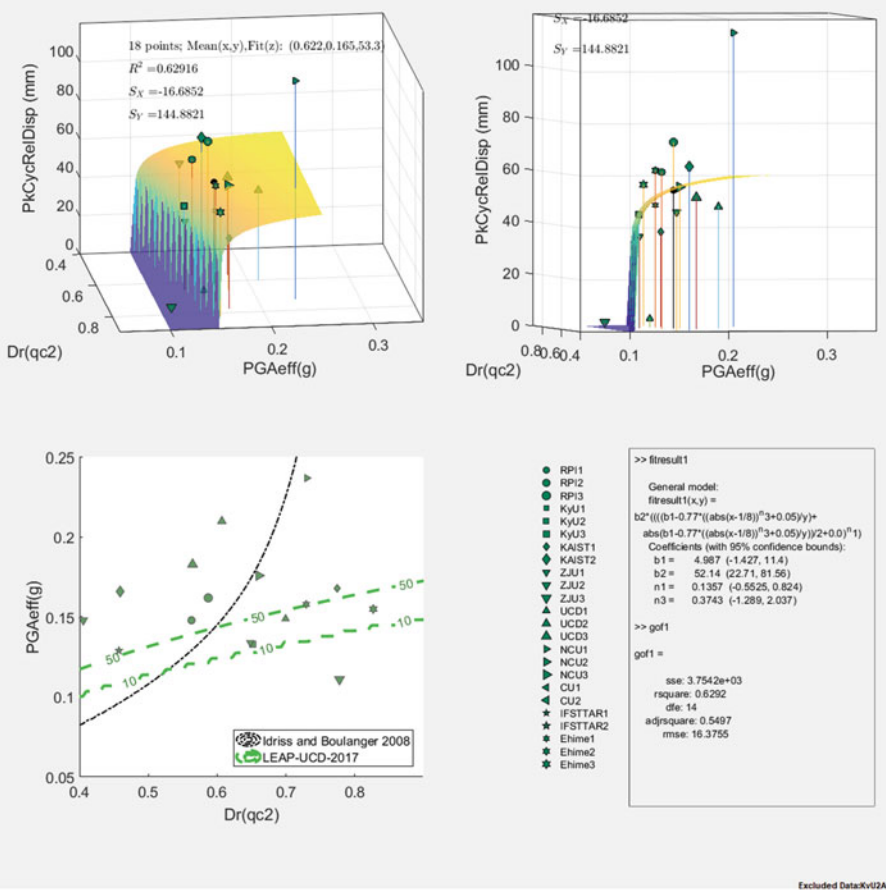

Fig. 4.19 Correlation between peak cyclic relative displacement between surface accelerometers and the base as a function of PGA_{eff} and $D_r(q_c(2\text{ m}))$. 19 of 20 experiments with requisite data are plotted (one outlier was excluded), and $R^2 = 0.66$. Panel (**a**) shows a contour plot; panel (**b**) shows a side view of the function. The same six-parameter model was used (Eq. 4.5)

triggered and relative displacements are 40–80 mm (in most cases) where liquefaction was triggered.

In a theoretical special case of complete liquefaction, the base might be expected to move while the ground surface was isolated from the base motion; hence, the relative cyclic displacement would equal the base cyclic displacement. The average peak of the 1 Hz component of the input base motion listed in Table 4.2b is 0.12 g. This acceleration corresponds to a cyclic displacement of ±39 mm. As is apparent in Fig. 4.19, the measured cyclic relative displacements are typically in the range of 40–80 mm—significantly greater than the base displacement. The relative displacement could be greater than the input base displacement if the surface displacements are of opposite phase to the base displacements and/or if the displacements are amplified at the ground surface.

In one case cyclic displacements were significantly greater than 80 mm; NCU1 displayed relative displacements of 113 mm (see Fig. 4.19 and/or Table 4.2c); the large relative displacement in NCU1 is at least partly explained by the fact that the 1 Hz component of the input base acceleration for NCU1 0.18 g is about 50% greater than the average 1 Hz component (0.12 g) listed in Table 4.2b. The relatively large amplitude of the low-frequency component of the base displacement for NCU1 helps explain why the cyclic displacements are the greatest for NCU1.

It should also be recalled that, due to the mechanical nature of the shaker at Ehime University, the Ehime motions contained a significant lower-frequency displacement that is very apparent for Ehime3 in Fig. 4.10.

4.10 Summary and Conclusions

The first goal of this paper is to provide an overview of all the experimental data from centrifuge testing for LEAP-UCD-2017. This overview will allow readers to quickly scan through the key time series data and various performance measures to evaluate the extent of liquefaction in various experiments. The second goal of this paper is to demonstrate that the experiments are consistent with each other and that they define a response function or trend between key input parameters and key liquefaction response parameters.

Time series data from input accelerations, accelerations and pore pressures in the central array and relative cyclic displacements obtained by integration of accelerations in the time domain are qualitatively compared. Residual displacements are characterized by the measured displacement from surface markers. Contour plots of lateral displacement and settlements of the surface markers are presented. Key density measures, cone penetration data, ground motion intensity measures, and response parameters are tabulated for all 24 experiments in Tables 4.2a, 4.2b, and 4.2c. All of the data in Tables 4.2a, 4.2b, and 4.2c and more data not presented here are also available in a spreadsheet document archived in the LEAP-UCD-2017 data archive in the NHERI DesignSafe (Kutter et al. 2018b). The results from Tables 4.2a, 4.2b, and 4.2c are cross plotted in 3D plots along with nonlinear regression surfaces to show the trend and to estimate the degree of correlation of the data to the response surface.

The consistency of the centrifuge experiments performed for LEAP-UCD-2017 is demonstrated by showing that responses (permanent displacement, duration of liquefaction, and the amplitude of the cyclic displacements observed in different experiments) are highly correlated to key parameters describing the resistance to liquefaction (e.g., relative density and cone penetration resistance) and the base motion shaking intensity measures (e.g., PGA, $PGA_{effective}$, and CAV_5).

The extent of liquefaction in the experiments is more highly correlated to the dry density correlated with cone penetration resistance than the dry density determined by direct measurement of mass and volume of the models, partly due to uncertainties and errors in direct density measurement. Errors in volume measurement arise due to the fact that the surfaces of the model are rough, sloped, and curved. Errors in

measurement of container dimensions, sand surface location, and resolution and accuracy of load cells used to measure the weight of the container combine to produce inaccurate density measurements.

The correlation between dry density and cone penetration resistance is obtained by linear regression between dry density determined from mass and volume measurements and q_c at a depth of 2 m. Then, the densities of the models are obtained from the measured q_c and the inverse linear regression line.

The PGA of the recorded base acceleration was found to be very sensitive to high-frequency components of the base motion, which varied significantly from facility to facility. The response of the model on the other hand was more sensitive to the lower frequency components of the input motion. Thus PGA was not a good parameter to use to describe the shaking intensity.

$PGA_{effective} = PGA_{1Hz} + 0.5\ PGA_{HighFrequency}$ was arbitrarily guessed as a trial function to help researchers at different facilities decide the appropriate input motions given the unique high-frequency noise produced by their centrifuge shakers. As it turned out, $PGA_{effective}$ is much more highly correlated to model response than is PGA. Another, less arbitrary intensity measure, cumulative absolute velocity (CAV_5), was also a good predictor of the duration of high excess pore pressures in the model.

Suggested measures of liquefaction response for this and future LEAP exercises are robust and easily and accurately measured and meaningful indicators of liquefaction phenomena. Until each facility can demonstrate that accurate measurements of surface markers using photographic or other scanning procedures, direct measurement of permanent displacements (especially lateral spreading and settlements) should be made using rulers, calipers, and surface markers. The displacements vary with position in the models; markers near the boundaries (end walls and side walls) are restricted by the boundaries. Displacements should be made near the boundaries and far from the boundaries to help assess boundary effects.

The duration of liquefaction of the top pore pressure sensor of a uniform soil deposit is proposed as a robust and useful indicator of the extent of liquefaction. This parameter is meaningful because the volume change of the soil deposit will be correlated to the duration of high pore pressures near the drainage boundary; the rate of volume change may be estimated using the water exit velocity from Darcy's law, $v = ki$. The maximum pore pressure ratio, $r_u = \Delta u/\sigma'_{vo}$, is theoretically an important pore pressure intensity measure, but it is less robust because it is sensitive to errors in the estimation of the depth of the sensor and corresponding initial effective stress.

Until non-contact methods such as photography and stereo photogrammetry are developed for more accurate measurement of time series of boundary displacements, the cyclic component relative displacement should be used as an indicator of the magnitude of cyclic strains induced by the shaking. The cyclic relative displacements of a layer may be obtained by subtracting displacements of the top and bottom of the layer obtained by integration of acceleration records at the top and bottom of the layer. The magnitude of cyclic strains has been shown to correlate well with liquefaction because strain levels change drastically during the onset of liquefaction.

LEAP-UCD-2017 produced an unprecedented quantity of model tests of sloping ground with intentionally varying input motions and soil density. Through data

analysis summarized in this paper, we have shown a repeatable response function between liquefaction response and key input parameters including shaking intensity and relative density. The repeatability of this response function proves that the results are consistent with each other within a range of uncertainty. The matrix of test results is sufficient to not only quantify the median response but also the sensitivity of response to variations in the input parameters and the centrifuge-centrifuge variability of the experimental results. The credibility of the data provided by demonstrated interlaboratory consistency allows us to move forward with meaningful use of this data for assessment of the accuracy of numerical simulation procedures. Since we have mapped out an experimental response surface with some ability to quantify experiment-experiment variability, it is recommended that the numerical procedures also be required to map out the same response surfaces.

It should be emphasized that many of the LEAP experiments included a total of two or three destructive motions. This paper focuses on results from the first motion only. Papers by each experiment facility describe the results from subsequent destructive motions.

Acknowledgments The experimental work on LEAP-UCD-2017 was supported by different funds depending mainly on the location of the work. The work by the US PI's (Manzari et al. 2017) is funded by National Science Foundation grants: CMMI 1635524, CMMI 1635307, and CMMI 1635040. The work at Ehime U. was supported by JSPS KAKENHI Grant Number 17H00846. The work at Kyoto U. was supported by JSPS KAKENHI Grant Numbers 26282103, 5420502, and 17H00846. The work at Kansai U. was supported by JSPS KAKENHI Grant Number 17H00846. The work at Zhejiang University was supported by National Natural Science Foundation of China (Nos. 51578501 and 51778573), Zhejiang Provincial Natural Science Foundation of China (LR15E080001), and National Basic Research Program of China (973 Project) (2014CB047005). The work at KAIST was part of a project titled "Development of performance-based seismic design," funded by the Ministry of Oceans and Fisheries, Korea. The work at NCU was supported by MOST: 106-2628-E-008-004-MY3.

References

Bolton, M. D., Gui, M. W., Garnier, J., Corte, J. F., Bagge, G., Laue, J., & Renzi, R. (1999). Centrifuge cone penetration tests in sand. *Geotechnique, 49*(4), 543–552.

Carey, T. J., Gavras, A., & Kutter, B. L. (2019a). Comparison of LEAP-UCD-2017 CPT results. In B. Kutter et al. (Eds.), *Model tests and numerical simulations of liquefaction and lateral spreading: LEAP-UCD-2017*. New York: Springer.

Carey, T. J., Stone, N., Bonab, M. H., & Kutter, B. L. (2019b). LEAP-UCD-2017 Centrifuge Test at University of California, Davis. In B. Kutter et al. (Eds.), *Model tests and numerical simulations of liquefaction and lateral spreading: LEAP-UCD-2017*. New York: Springer.

Carey, T. J., Stone, N., & Kutter, B. L. (2019c). Grain size analysis and maximum and minimum dry density of Ottawa F-65 sand for LEAP-UCD-2017. In B. Kutter et al. (Eds.), *Model tests and numerical simulations of liquefaction and lateral spreading: LEAP-UCD-2017*. New York: Springer.

Carey, T., Stone, N., Kutter, B., & Hajialilue-Bonab, M. (2018a). A new procedure for tracking displacements of submerged sloping ground in centrifuge testing. In *Proceedings of 9th International Conference on Physical Modelling in Geotechnics, ICPMG 2018* (Vol. 1, pp. 829–834). London: CRC Press/Balkema.

Carey, T., Gavras, A., Kutter, B., Haigh, S. K., Madabhushi, S. P. G., Okamura, M., Kim, D. S., Ueda, K., Hung, W.-Y., Zhou, Y.-G., Liu, K., Chen, Y.-M., Zeghal, M., Abdoun, T., Escoffier,

S., & Manzari, M. (2018b). A new shared miniature cone penetrometer for centrifuge testing. In *Proceedings of 9th International Conference on Physical Modelling in Geotechnics, ICPMG 2018* (Vol. 1, pp. 293–229). London: CRC Press/Balkema.

El Ghoraiby, M. A., Park, H., & Manzari, M. T. (2017). *LEAP 2017: Soil Characterization and Element Tests for Ottawa F65 Sand*. Washington, DC: George Washington University.

Idriss, I. M., & Boulanger, R. W. (2008). *Soil Liquefaction During Earthquakes, MNO-12* (p. 142). Oakland, CA: Earthquake Engineering Research Institute.

Kutter, B. L., Carey, T. J., Bonab, M. H., Stone, N., Manzari, M., Zeghal, M., Escoffier, S., Haigh, S., Madabhushi, G., Hung, W., Kim, D., Kim, N., Okamura, M., Tobita, T., Ueda, K., & Zhou, Y. (2019). LEAP-UCD-2017 V. 1.01 model specifications. In B. Kutter et al. (Eds.), *Model tests and numerical simulations of liquefaction and lateral spreading: LEAP-UCD-2017*. New York: Springer.

Kutter, B. L., Carey, T. J., Hashimoto, T., Zeghal, M., Abdoun, T., Kokkali, P., Madabhushi, S. P. G., Haigh, S. K., Burali d'Arezzo, F., Madabhushi, S. S. C., Hung, W.-Y., Lee, C.-J., Cheng, H.-C., Iai, S., Tobita, T., Ashino, T., Ren, J., Zhou, Y.-G., Chen, Y., Sun, Z.-B., & Manzari, M. T. (2017). LEAP-GWU-2015 experiment specifications, results, and comparisons. *International Journal of Soil Dynamics and Earthquake Engineering, Elsevier, 113*, 616. https://doi.org/10.1016/j.soildyn.2017.05.018.

Kutter, B. L., Carey, T. J., Zheng, B. L., Gavras, A., Stone, N., Zeghal, M., Abdoun, T., Korre, E., Manzari, M., Madabhushi, G. S., Haigh, S., Madabhushi, S. S., Okamura, M., Sjafuddin, A. N., Escoffier, S., Kim, D.-S., Kim, S.-N., Ha, J.-G., Tobita, T., Yatsugi, H., Ueda, K., Vargas, R. R., Hung, W.-Y., Liao, T.-W., Zhou, Y.-G., & Liu, K. (2018a). Twenty-four centrifuge tests to quantify sensitivity of lateral spreading to Dr and PGA. In S. J. Brandenberg & M. T. Manzari (Eds.), *Geotechnical Earthquake Engineering and Soil Dynamics V, GSP 293* (pp. 383–393). Alexandria, VA: ASCE. https://doi.org/10.1061/9780784481486.040.

Kutter, B., Zeghal, M., Manzari, M. (2018b). *LEAP-UCD-2017 Experiments (Liquefaction Experiments and Analysis Projects)*, DesignSafe-CI [publisher], Dataset. https://doi.org/10.17603/DS2N10S

Manzari, M., Ghoraiby, M. E., Kutter, B. L., Zeghal, M., Abdoun, T., Arduino, P., Armstrong, R. J., Beaty, M., Carey, T., Chen, Y.-M., Ghofrani, A., Gutierrez, D., Goswami, M., Haigh, S. K., Hung, W.-Y., Iai, S., Kokkali, P., Lee, C.-J., Madabhushi, S. P. G., Mejia, L., Sharp, M., Tobita, T., Ueda, K., Zhou, Y.-G., & Ziotopoulou, K. (2017). Liquefaction analysis and experiment projects (LEAP): Summary of observations from the planning phase. *International Journal of Soil Dynamics and Earthquake Engineering, 113*, 714. https://doi.org/10.1016/j.soildyn.2017.05.015.

Parra Bastidas A.M., Boulanger, R.W., Carey, T., DeJong, J. (2017) Ottawa F-65 Sand Data from Ana Maria Parra Bastidas, https://datacenterhub.org/resources/ottawa_f_65, doi: 10.17603/DS2MW2R.

Yoshimine, M., Nishizaki, H., Amano, K., & Hosono, Y. (2006). Flow deformation of liquefied sand under constant shear load and its application to analysis of flow slide in infinite slope. *Soil Dynamics and Earthquake Engineering, 26*, 253–264.